A new model of mass flow characteristics in electronic expansion valves considering metastability

Chen Liang*, Liu Jinghui, Chen Jiangping, Chen Zhijiu

School of Mechanical Engineering, Shanghai Jiaotong University, Shanghai 200240, China

ABSTRACT

This paper presents an experimental study on the mass flow characteristics of electronic expansion valves in a wide operating condition range. It was found that flow choking always occurs under common operating conditions in refrigeration systems. Based on metastability in EEVs, a new model predicting mass flow rate was proposed under flow choking conditions. Different from the conventional models using Bernoulli equation which employed downstream pressure at the EEV exit and a corrected mass flow coefficient, the present model considered metastable liquid flow caused by rapid depressurization, and employed single-phase incompressible flow coefficient and metastable pressure at the throat. An empirical correlation of the metastable pressure, based on the experimental data for R22 and its substitutes, R407C and R410A, was developed in a power law form of dimensionless parameters including upstream operating parameters and refrigerant thermophysical properties and throat area. The predictions of the present model were found to be in good agreement with the measured data, and approximately 95% of the measured data fall within a relative deviation of ±7.0%. The comparison with a prior model shows that, in terms of flashing mechanism application and predicting accuracy, the present model is better than the conventional model without considering metastability.

© 2008 Elsevier Masson SAS. All rights reserved.

1. Introduction

The electronic expansion valve, driven by a stepping motor controlled by a pulse signal generator, has been widely applied in refrigeration systems. The stepping motor can afford a precise adjustment to valve opening, for instance, an EEV with full opening of 500 pulses and orifice diameter of 1.8 mm can reach a precision up to 0.002 mm^2 of throat area per one pulse signal. Due to precise and fast control for refrigerant flow, the refrigeration systems using EEVs have much more advantages than those using conventional expansion devices in terms of refrigerant supplying stability and superheat hunting reduction. The study results [1] showed that EEV can achieve a higher COP under transient conditions and a better control for superheat under steady-state conditions in comparison with TXV, chiefly with non-azeotropic blends as working fluids. The EER of an air conditioning plant using EEV is higher than using TXV, because EEV can execute a better control strategy and has a more steady operation [2]. Furthermore, under off-design charging conditions, the EEV systems have much better stability as compared with the capillary tube systems [3]. In general, almost all benefits of EEVs can be attributed to precise flow metering or precise opening adjustment. Further improve-

ment upon the opening adjustment precision is supposed to be made by increasing the pulse number of full opening, for instance, a better precision of 0.0015 mm^2 per one pulse can be achieved by full opening of 2000 pulses. The high precision of EEV is due to the application of the stepping motor controlling the valve opening, and the opening can be available from the pulse number of the stepping motor, whereas other expansion valves are not so as EEV. The feature makes it possible to model mass flow rate of EEV at different valve openings. The incompressible single-phase fluid equation derived from Bernoulli equation was usually adopted to depict the mass flow rate in many open literatures [4–7], which is expressed as

$$\dot{m} = C_d A_{\text{th}} \sqrt{2\rho_l (P_{\text{up}} - P_{\text{down}})} \tag{1}$$

where $\dot{m}$ is the mass flow rate, A_{th} the geometric throat area can be determined by the pulse number of the stepping motor, ρ_l is the inlet density of working fluid, P_{up} and P_{down} are the upstream and downstream pressures, respectively, C_d is the mass flow coefficient which is a constant for incompressible single-phase fluids.

Since phase transition occurs when refrigerant flows through EEVs and flow mechanisms inside EEVs have not been fully understood, the mass flow coefficient C_d was usually corrected with the parameters related to EEVs in previous researches. Wile [4] first suggested an equation for C_d of TEVs which was correlated with inlet and outlet thermophysical properties of refrigerant. Ma et al. [5], Zhang [6] and Park et al. [7] proposed three more accurate

* Corresponding author. Tel.: +086 02134206087; fax: +086 02134206087.
E-mail address: chenliang_sjtu@yahoo.com.cn (L. Chen).

Nomenclature

A_{th}	geometric throat area	mm^2
C	coefficient in Eq. (7)	
C_d	corrected flow coefficient	
C_D	single-phase flow coefficient	
C_{meta}	degree of metastability	
$C_{p,l}$	specific heat	kJ kg^{-1} K^{-1}
COP	coefficient of performance	
D	orifice diameter	mm
D_e	equivalent diameter	mm
e_i	exponents of Pi-groups	
E	deviation	
EER	energy efficiency ratio	BTU Watt^{-1} h^{-1}
EEV	electronic expansion valve	
IHE	isentropic homogeneous equilibrium	
$\dot{m}$	mass flow rate	kg h^{-1}
P	absolute pressure	MPa
P_c	critical pressure	MPa
T_c	critical temperature	K
T_{sc}	subcooling	°C
TXV	thermostatic expansion valve	

Greek symbols

π	dimensionless parameter	
σ	surface tension	mN m^{-1}
ρ	density	kg m^{-3}
μ	viscosity	μPa s

Subscripts

aver	average
cond	condensation
down	downstream
evap	evaporation
l	liquid
meas	measured
meta	metastability
p	constant pressure
pred	predicted
rel	relative
sat	saturation
sc	subcooling
up	upstream
th	throat

equations for C_d related to geometry, inlet and outlet operating conditions and refrigerant thermophysical properties. In their studies, the EEV was investigated as a black box and the mass flow coefficient was fitted using the experimental data related to both inlet and outlet of EEV.

Bernoulli equation cannot clearly depict the throttling mechanism of EEVs and has limitation to model two-phase mass flow characteristics. Davies and Daniels [8] and Zhang et al. [9] developed empirical correlations of $\dot{m}$ based on the experimental data to predict the mass flow rate directly. Considering the actual mass flow rate is usually larger than that calculated by IHE Model because of the effect of metastable phenomenon, Liu et al. [10] developed a new model to investigate the mass flow characteristics on the basis of choking assumption, in which a Homogeneous Equilibrium Fluid Model and a Frozen Flow Model were employed to define a metastability coefficient used to depict the flow characteristics of EEV.

The flashing mechanisms are important in the research of flow characteristics and have a great influence on prediction of the mass flow rate in EEVs. An improvement is supposed to be made, if Bernoulli equation is combined with the actual flashing mechanisms. In this study, a new model to improve on the previous models using Bernoulli equation, considering metastability in EEVs based on the experimental data with R410A, R22 and R407C as working fluids, was developed to model the mass flow rate.

2. Analyses of flashing mechanisms in EEVs

The flashing mechanisms of different flow restrictions have been studied in many literatures. For short orifice tube, Kim and O'Neal [11] showed the existence of metastable liquid region inside it. For nozzle, the investigated results afforded by Schrock et al. [12], Alamgir and Lienhard [13] and Abuaf et al. [14] revealed the thermodynamic behaviors of critical two-phase flow discharge with rapid depressurization in convergent-divergent nozzles and, that flashing inception point of initially subcooled liquid is just located at the throat. Vieira and Simões-Moreira [15] showed many Schlieren images of the metastable liquid core surrounded by shock wave structure in the flashing process of iso-octane at different degrees of metastability in short nozzles, the

presence of the metastable liquid at the exit of minimum area for initially subcooled liquid at high pressure ratios of inlet to outlet was verified by means of photographic observations.

In refrigeration systems, the inlet refrigerant of expansion devices is commonly subcooled liquid, and the flashing mechanisms of refrigerant through expansion devices are various with respect to different operating conditions. Simões-Moreira and Bullard [16] summarized three flashing mechanisms caused by different degrees of metastability. One of the three regimes, that flashing takes place on the surface of the liquid core through an evaporation wave process, occurs in short nozzles at a high degree of metastability when flow choking happens. The flow mechanisms of nozzles are supposed to be approximately identical with EEVs because the flow channel structures of EEVs seem very similar to nozzles and, the ratios of condensing pressure to evaporating pressure are commonly very high in refrigeration systems. The flow channel structure of EEV is shown in Fig. 1(a), and Fig. 1(c) is the enlarged drawing of valve orifice, and the schematic of convergent-divergent nozzle is shown in Fig. 1(b). As shown in Figs. 1(b) and 1(c), the cross-section area of the flow channel is gradually decreasing and increasing consecutively along the flow path for both EEV and nozzle. The flashing process when choking occurs in EEV is graphically shown in Fig. 1(c): a rapid depressurization makes the liquid refrigerant become superheated at the throat of EEV when subcooled refrigerant from high-pressure condenser flows through EEV into low-pressure evaporator, and then the superheated refrigerant explosively flashes in a discontinuous process with an evaporation wave appearing, the evaporation wave discontinuity is dynamic and oblique to the main superheated refrigerant velocity, which was called oblique evaporation wave by Simões-Moreira [17]. The superheated refrigerant is evaporated resulting in a high-speed two-phase mixture flow, and then the two-phase flow reaches sonic speed and continues expanding up to supersonic speed, eventually the expansion process is terminated through a shock wave with an abrupt pressure rise. Thus, according to the flashing mechanism analyses, the mass flow rate of the metastable liquid at the throat of EEV can be modeled by using Bernoulli equation in the stage before phase transition. As for possible sporadic nucleation taking place within the metastable liquid, the modeling method can also be available according to the con-
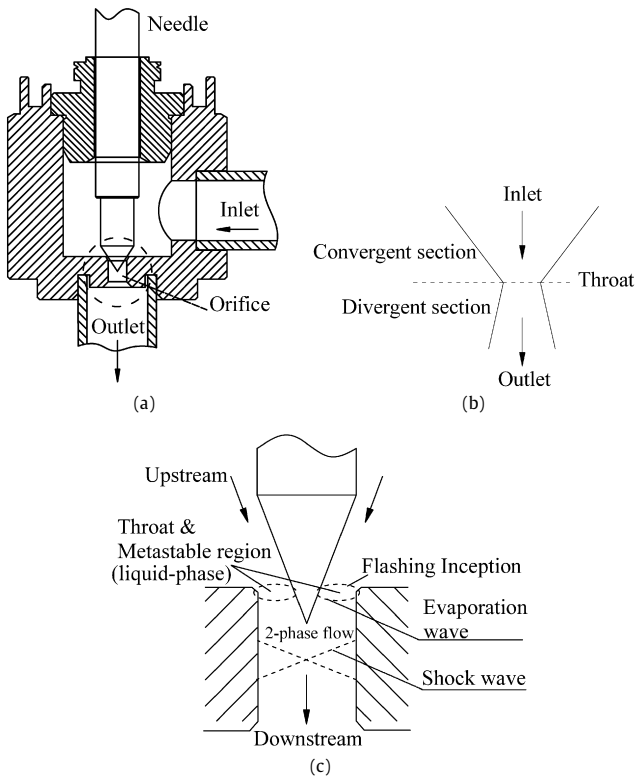
Fig. 1. The schematic of the flow passages in EEV and nozzle. (a) The structure of flow passage in EEV. (b) Diagram of the convergent-divergent nozzle. (c) The schematic of flashing process in the valve orifice.

clusions from Schrock et al. [12], Alamgir and Lienhard [13] and Abuaf et al. [14] that void development upstream the throat can be negligible for the critical flashing flow of initially subcooled liquid. The similar method has been practiced in other expansion devices, for instance, Aaron and Domanski [18] used Bernoulli equation to depict the R22 mass flow rate through short tubes, in which the pressure before the flashing inception point was employed. On the precondition that the flashing inception occurs immediately at the

throat of EEVs under flow choking conditions, a corrected form of Eq. (1) is expressed as

$$\dot{m} = C_D A_{th} \sqrt{2\rho_l (P_{up} - P_{th})} \tag{2}$$

where P_{th} is the metastable liquid pressure at the throat, ρ_l can be obtained from REFPROP [25], C_D is the mass flow coefficient of single-phase fluid, which is a constant. The experimental data from Brown et al. [12,19], Sozzi and Sutherland [20], Zimmer et al. [21], Simoneau and Hendricks [22] showed that C_D was in a range of 0.94 ± 0.04, quite close to the ideal single-phase value. In this paper, the nozzle discharge coefficient correlation given by Vieira and Simões-Moreira [15] was adopted in EEV to calculate the C_D, which is represented as

$$C_D = 0.9673 - 5.6682/\sqrt{R_e} \tag{3}$$

where R_e is the inlet Reynolds number based on the equivalent diameter of the throat area. The calculated values of C_D in Eq. (3) scatter in a range of 0.956 ± 0.001 according to the experimental data, and an average value 0.956 was used in this study. The maximal deviations of some calculated parameters caused by choosing different values of C_D in the range of 0.956 ± 0.001, such as for the calculations of $\dot{m}$ in Eq. (2) and P_{th} in Eq. (5), are both less than 0.18%. Thus, if the pressure P_{th} is known, the mass flow rate of EEVs can be calculated through Eq. (2). In this paper, the pressure at the throat was determined by multivariable regression using the experimental data.

3. Experimental apparatus

The experimental setup shown in Fig. 2 was used to test the performance of EEVs, and the tested EEV sample was installed between an condenser and an evaporator. The condensing pressure (upstream pressure) was controlled by adjusting cooling water flow rate, and the evaporating pressure (downstream pressure) was controlled by adjusting wet and dry bulb temperatures of Air Handling Unit and rotating speed of an inverter-driven compressor. The upstream subcooling of EEV was adjusted by controlling refrigerant charge with an accumulator installed between the condenser and EEV.

The operating condition data of EEV were obtained through temperature sensors, pressure transducers and an mass flow meter.
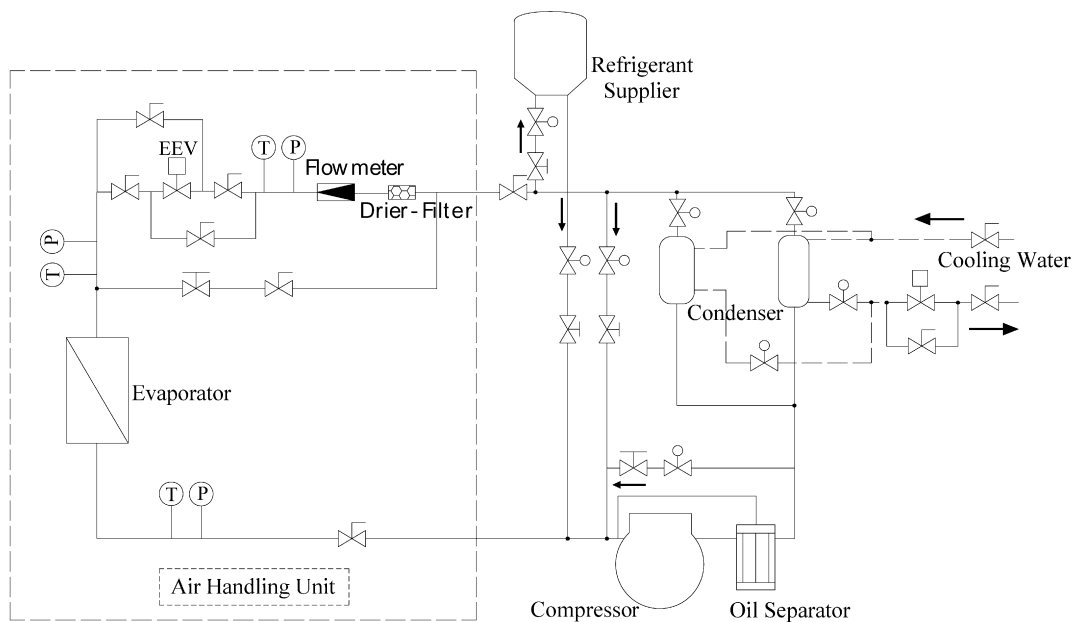
Fig. 2. The schematic of EEV test rig.

The temperatures were monitored with thermocouples according to ASHRAE Standard 41.1 [23], and the refrigerant pressures were measured according to ASHRAE Standard 41.3 [24]. The mass flow meter was installed between the condenser and EEV. Each sensor was calibrated to reduce experimental uncertainty. The specifications and uncertainties of the measuring instruments were summarized in Table 1.

The test data used for model development consisted of two data sources, that is, the data obtained by the current test rig using samples of EEV #1, #2 and #3 working with R410A, and the measured data presented by Zhang [6] using EEV #4 with R22 and R407C as working fluids. The two data sources covered a wide range of operating conditions and different EEV geometric structures listed in Table 2. All the tested EEVs had the inlet and outlet chamferings of the same depth and angle, and were attached to the tubes with inner diameter of approximately 8.0 mm. The EEV was driven by a stepping motor controlled by a pulse signal generator, and the opening of EEV was represented by the pulse number of the stepping motor in this paper, for example, in Fig. 4, 200 pulse means the opening of the tested EEV is 200 pulses. The test procedure commonly took about 0.5–1.0 h to reach a steady state and thereafter, the data were recorded every 10 s and averaged for a period of 5 min.

4. Experimental investigation of metastability for EEVs

The metastable liquid arises in the flashing process inside expansion devices while flow choking occurs. In refrigeration systems, the most running conditions can always reach the choking conditions of EEVs [10], and choking behavior commonly happens along with the presence of shock wave. Simões-Moreira and Bullard [16] found that shock wave associated with flashing jet at extreme pressure drop conditions in the flow restrictions is typically found in refrigeration systems, that is, flow choking also occurs simultaneously. In this study, the EEV tests were performed in a wide range of operating conditions, beyond the common running condition range in refrigeration systems, to investigate whether flow choking occurs. If choking occurs, the calculation prerequisite to apply Eq. (2) is definitely satisfied. To evaluate metastability, a dimensionless degree-of-metastability parameter was defined and expressed as

$$C_{\text{meta}} = \frac{P_{\text{sat}} - P_{\text{th}}}{P_{\text{sat}}} \tag{4}$$

where P_{sat} is the saturation pressure corresponding to inlet temperature, P_{th} is difficult to measure directly for short and narrow space at the throat in EEVs, but it can be calculated indirectly and derived from Eq. (2) as

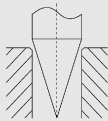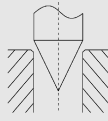$$P_{\text{th}} = P_{\text{up}} - \frac{\dot{m}^2}{2\rho_l C_D^2 A_{\text{th}}^2} \tag{5}$$
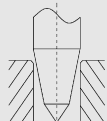
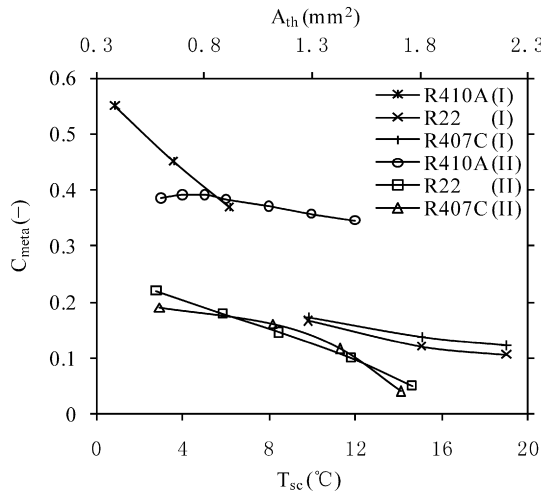where P_{up} and $\dot{m}$ can be measured in the EEV tests.

The parameter C_{meta} can also be regarded as an index evaluating pressure loss as the metastable liquid flows through the throat of EEV. The values of C_{meta} obtained by calculation of Eq. (4) are in the ranges from 0.28 to 0.67 for R410A, from 0.05 to 0.35 for R22, and from 0.05 to 0.34 for R407C in the operating conditions listed in Table 2, so it can be verified the existence of the metastable liquid. Figs. 3 and 4 show the variations of the dimensionless degree-of-metastability with throat area, subcooled temperature, upstream and downstream pressures for R410A, R22 and R407C, respectively. In general, the curves of the three refrigerants have the similar trends, but the values of C_{meta} for R410A are higher than that for R22 and R407C because saturation pressure of R410A is greater than the other two refrigerants corresponding to a given inlet temperature. As can be observed in Figs. 3 and 4 (curve family I), under the constant downstream pressures, the C_{meta} decreases with the throat area increasing because the descent of flow restriction leads to a reduction of pressure loss, and the C_{meta} also decreases with more subcooling mainly because a decrease in saturation pressure corresponding to inlet temperature causes a less pressure loss, and an increase of the C_{meta} can be found as the upstream pressure increases due to an increase in pressure loss. The variations of the dimensionless degree-of-metastability with the downstream pressure at the opening of 200 and 400 pulses in Fig. 4 (curve family II) illustrate the relations between metastability and choking flow characteristics. The choices of the opening of 200 and 400 pulses are mainly because the opening range is frequently used in refrigeration systems. As can be observed, the

Table 1
Specifications and uncertainties of the measuring instruments.

Item	Full scale	Uncertainty	Model
Temperature sensor (T type thermocouple)	-50–300 °C	± 0.15 °C	Pt-RTD
Pressure transducer	4500 kPa	$\pm 0.25\%$ of full scale	PTX7518
Mass flow meter (Coriolis meter)	600 kg h^{-1}	$\pm 0.1\%$ of full scale	CN025C-SS

Table 2
Experimental conditions in this study.

	Model no.	#1	#2	#3		#4
EEV	Flow passage geometry					
	Full opening (pulse)	500	480	500		500
	Orifice diameter (mm)	1.8	1.8	1.65		1.8
	pitch on screw (mm)	0.6	0.5	0.5		0.6
	Conical angle (degree)	20.0	24.70	8.25	96	27.40
	Needle length (mm)	3.0	1.6	1.9	0.7	2.9
	Orifice length (mm)	2.7	2.7	3.0		3.1
Working fluid			R410A			R22/R407C
Test condition	Condensing pressure (MPa)	2.10–3.60				1.14–1.96
	Evaporating pressure (MPa)	0.54–1.50				0.54–1.10
	Subcooling (°C)	2–22				2–15
	Throat area (mm^2)	0.32–1.75				0.62–2.45
	Tested mass flow rate (kg h^{-1})	55.7–325.5				55.9–264.8
	Number of test data	70				50/50

(I) Test conditions for $C_{meta}\sim A_{th}$ curves:
R410A: P_{cond}=2.40 MPa, P_{evap}=0.85 MPa, T_{sc}=5 ℃
R22: P_{cond}=1.20 MPa, P_{evap}=0.69 MPa, T_{sc}=5 ℃
R407C: P_{cond}=1.14 MPa, P_{evap}=0.62 MPa, T_{sc}=5 ℃

(II) Test conditions for $C_{meta}\sim T_{sc}$ curves:
R410A: P_{cond}=3.10 MPa, P_{evap}=0.70 MPa, 200 pulse
R22: P_{cond}=1.53 MPa, P_{evap}=0.69 MPa, 200 pulse
R407C: P_{cond}=1.50 MPa, P_{evap}=0.62 MPa, 200 pulse

Fig. 3. The dimensionless degree of metastability with respect to throat area (I) and subcooling (II).
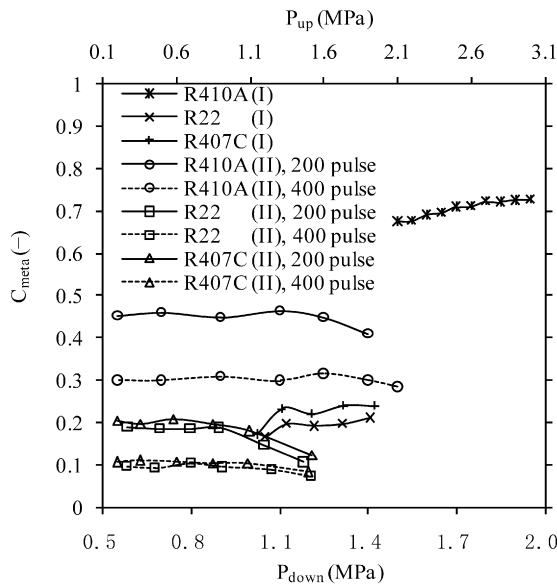
(I) Test conditions for $C_{meta}\sim P_{up}$ curves:
R410A: P_{evap}=0.80 MPa, T_{sc}=5 ℃, 200 pulse
R22: P_{evap}=0.68 MPa, T_{sc}=5 ℃, 200 pulse
R407C: P_{evap}=0.62 MPa, T_{sc}=5 ℃, 200 pulse

(II) Test conditions for $C_{meta}\sim P_{down}$ curves:
R410A: P_{cond}=3.10 MPa, T_{sc}=5.0 ℃
R22: P_{cond}=1.72 MPa, T_{sc}=6.5 ℃
R407C: P_{cond}=1.72 MPa, T_{sc}=6.5 ℃

Fig. 4. The dimensionless degree of metastability with respect to upstream pressure (I) and downstream pressure (II).

dimensionless degree-of-metastability increases with the downstream pressure decreasing at first as the relatively high pressure downstream, beyond the common evaporating temperature range,

Table 3
Definitions of the dimensionless Pi-groups.

Pi-group	Parameter	Consideration
π_1	$\frac{P_{up}}{P_c}$	Upstream pressure
π_2	$\frac{T_{sc}}{T_c}$	Subcooling
π_3	$\frac{\rho_l}{1000 P_{up}/(C_{p,l} T_c)}$	Inlet liquid density
π_4	$\frac{\mu_l}{D_e \sqrt{\rho_l P_{up}} \cdot 10^6}$	Inlet liquid viscosity
π_5	$\frac{D_e}{D}$	Throat area
π_6	$\frac{P_{th}}{P_c}$	Pressure at the throat

cannot trigger flow choking yet, and then it becomes insensitive and finally independent to the downstream pressure below a certain value of the pressure, which is just a threshold leading to flow choking. The downstream threshold pressures of 200 and 400 pulses for R410A are about 1.2 and 1.3 MPa, and 0.9 and 1.1 MPa for both R22 and R407C, respectively. The saturated temperatures corresponding to these downstream threshold pressures are in a range from 16 to 24 °C, and the temperature range is much higher than the common evaporating temperatures in most refrigeration systems. It can also be seen that, when the opening is changed from 200 to 400 pulses, the downstream pressure threshold becomes greater whereas the C_{meta} becomes smaller. The reason for the phenomenon is that there is a relatively lower depressurization rate for greater throat area than for smaller one and, lower depressurization rate means higher metastable pressure and downstream pressure and therefore, the dimensionless degree-of-metastability is lower according to Eq. (4). According to the experimental analyses, it can be concluded that the refrigerant flow through EEV is commonly choked in refrigeration systems and in the meanwhile, the metastable liquid exists at the throat. Based on the conclusions, an empirical correlation used to calculate the mass flow rate under choking conditions can be developed.

5. Development of an empirical correlation for the pressure at the throat

The pressure at the throat of EEV is influenced by upstream operating parameters and refrigerant thermophysical properties and EEV geometries under choking conditions. All these parameters should be selected to develop the correlation based on the experimental data. The operating parameters considered in the study are P_{up} the upstream pressure and T_{sc} the upstream subcooling. Among the refrigerant properties, just density (ρ_l) and viscosity (μ_l) of the inlet liquid need to be considered, and they can be obtained from REFPROP [25]. Only the throat area among valve geometries listed in Table 2 has distinct effect on the mass flow rate, so the equivalent diameter (D_e) of the throat area is considered as a geometric parameter. The relationship between the pressure at the throat and these selected influencing variables has the following equation form:

$$P_{th} = f(P_{up}, P_c, T_{sc}, T_c, D_e, D, \rho_l, \mu_l, C_{p,l}) \qquad (6)$$

Six dimensionless Pi-groups were derived by combining the selected variables in Eq. (6) with the four repeating variables of P_c, T_c, D and $C_{p,l}$ based on the Buckingham Pi theorem [26]. The definitions of the six dimensionless Pi-groups (π_{1-6}) are shown in Table 3.

Figs. 5–7 show the influences of the five selected parameters in Table 3 on the dimensionless pressure at the throat. As can be seen, the dimensionless pressure at the throat is approximately proportional to P_{up}/P_c and D_e/D, and is conversely changed with respect to T_{sc}/T_c, $\frac{\rho_l}{1000 P_{up}/(C_{p,l} T_c)}$ and $\frac{\mu_l}{D_e \sqrt{\rho_l P_{up}}}$. These results can be explained as follows: for the curve family I in Fig. 5, the pres-
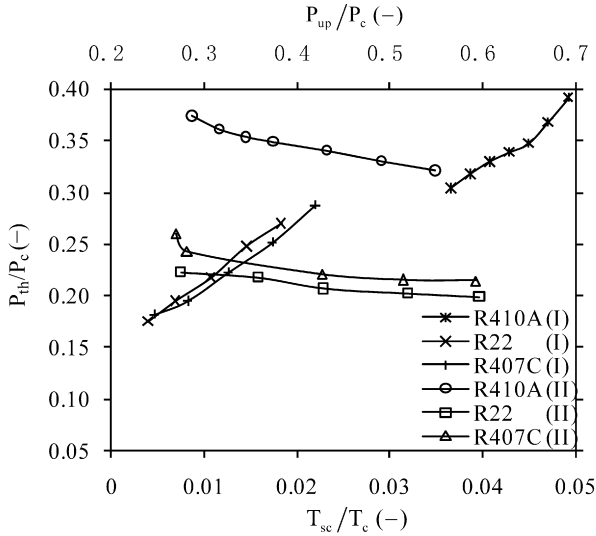
(I) Test conditions for dimensionless $P_{th} \sim P_{up}$ curves:
R410A: P_{evap}=0.70 MPa, T_{sc}=5 ℃, 200 pulse
R22: P_{evap}=0.68 MPa, T_{sc}=5 ℃, 200 pulse
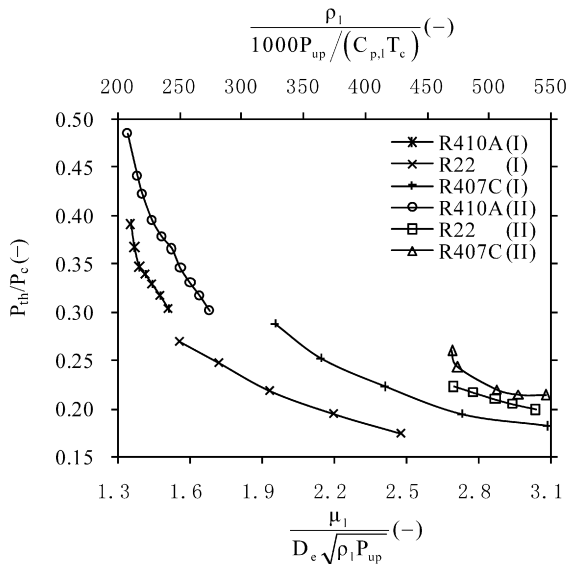R407C: P_{evap}=0.62 MPa, T_{sc}=5 ℃, 200 pulse

(II) Test conditions for dimensionless $P_{th} \sim T_{sc}$ curves:
R410A: P_{cond}=3.10 MPa, P_{evap}=0.70 MPa, 200 pulse
R22: P_{cond}=1.53 MPa, P_{evap}=0.69 MPa, 200 pulse
R407C: P_{cond}=1.50 MPa, P_{evap}=0.62 MPa, 200 pulse

Fig. 5. Effect of upstream pressure (I) and subcooling (II) on the pressure at the throat.

(I) Test conditions for dimensionless $P_{th} \sim \rho_l$ curves:
R410A: P_{evap}=0.70 MPa, T_{sc}=5 ℃, 200 pulse
R22: P_{evap}=0.68 MPa, T_{sc}=5 ℃, 200 pulse
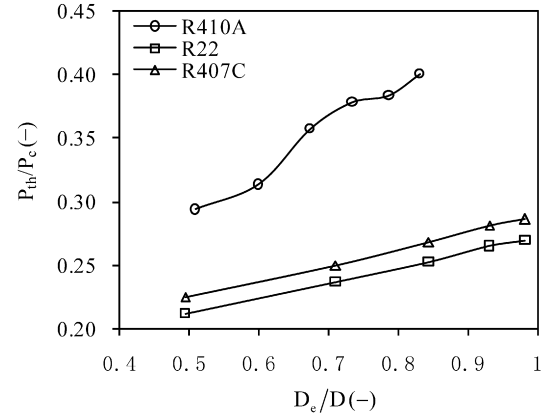R407C: P_{evap}=0.62 MPa, T_{sc}=5 ℃, 200 pulse

(II) Test conditions for dimensionless $P_{th} \sim \mu_l$ curves:
R410A: P_{cond}=3.50 MPa, P_{evap}=0.90 MPa, 200 pulse
R22: P_{cond}=1.53 MPa, P_{evap}=0.69 MPa, 200 pulse
R407C: P_{cond}=1.50 MPa, P_{evap}=0.62 MPa, 200 pulse

Fig. 6. Effects of inlet liquid density (I) and inlet liquid viscosity (II) on the pressure at the throat.

Test conditions:
R410A: P_{cond}=3.10 MPa, P_{evap}=0.90 MPa, T_{sc}=5.0 ℃
R22: P_{cond}=1.72 MPa, P_{evap}=0.58 MPa, T_{sc}=6.5 ℃
R407C: P_{cond}=1.72 MPa, P_{evap}=0.54 MPa, T_{sc}=6.5 ℃

Fig. 7. Effect of equivalent diameter on the pressure at the throat.

sure at the throat increases owing to the upstream pressure increasing; for the curve family II in Fig. 5, more subcooling means lower inlet temperature under a constant upstream pressure, and the corresponding saturation pressure decreases as consequence of lower inlet temperature so as to cause a decrease in the pressure at the throat; for the curve family I in Fig. 6, an increase in liquid density caused by a decrease in upstream pressure makes the metastable pressure decrease; for the curve family II in Fig. 6, more viscosity causes more pressure loss due to internal viscous friction, so the pressure at the throat becomes lower accordingly; in Fig. 7, an increase of the equivalent diameter leads to a reduction of pressure loss due to the descent of flow restriction, so the metastable pressure increases. Since saturation pressure of R410A is higher than R22 and R407C corresponding to a given temperature, the pressure at the throat is also higher than R22 and R407C accordingly in such figures. Thus, the dimensionless Pi-groups consisting of these selected parameters are all correlative to the dimensionless pressure at the throat. Consequently, a generalized correlation of Pi-groups can be expressed as

$$\pi_6 = C \cdot \pi_1^{e_1} \cdot \pi_2^{e_2} \cdot \pi_3^{e_3} \cdot \pi_4^{e_4} \cdot \pi_5^{e_5} \tag{7}$$

The coefficient (C) and the exponents (e_{1-5}) of the independent Pi-groups in Eq. (7) were determined by using a non-linear regression method with the experimental data. Finally, the generalized dimensionless correlation of the pressure at the throat for R410A, R22 and R407C was obtained as follows:

$$\pi_6 = 9.6681\pi_1^{0.4314}\pi_2^{-0.0844}\pi_3^{-0.4871}\pi_4^{0.0559}\pi_5^{0.2580} \tag{8}$$

6. Discussion of the model

The predicting model (8) was validated by relative deviation, average deviation and standard deviation between the measured data and the predicted mass flow rates, which are defined as follows, respectively.

$$\text{Relative deviation} = \frac{(\dot{m}_{pred} - \dot{m}_{meas})}{\dot{m}_{meas}} \times 100 \ (\%) \tag{9}$$

$$\text{Average deviation} = \frac{1}{n}\sum_1^n\left[\frac{(\dot{m}_{pred} - \dot{m}_{meas})}{\dot{m}_{meas}} \times 100\right] (\%) \tag{10}$$

$$\text{Standard deviation} = \sqrt{\frac{1}{n}\sum_1^n(E_{Rel} - E_{Aver})^2} \ (\%) \tag{11}$$
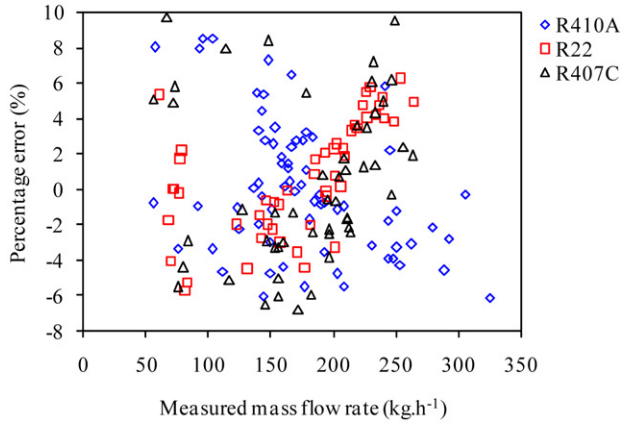
Fig. 8. Relative deviation versus the measured mass flow rate.
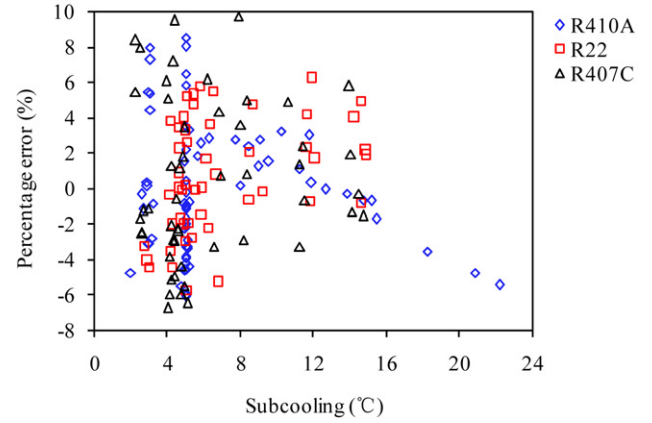

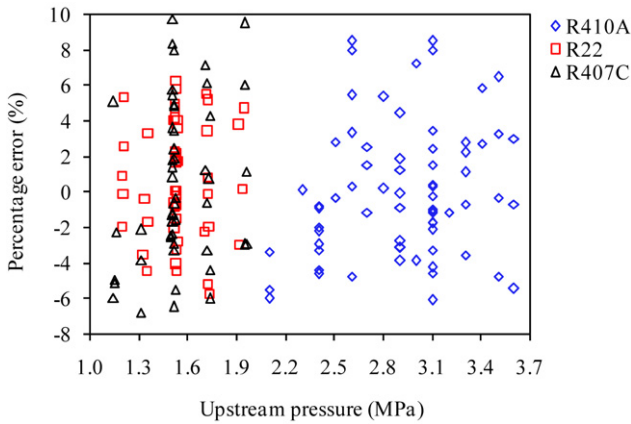**Fig. 10.** Relative deviation versus subcooling.

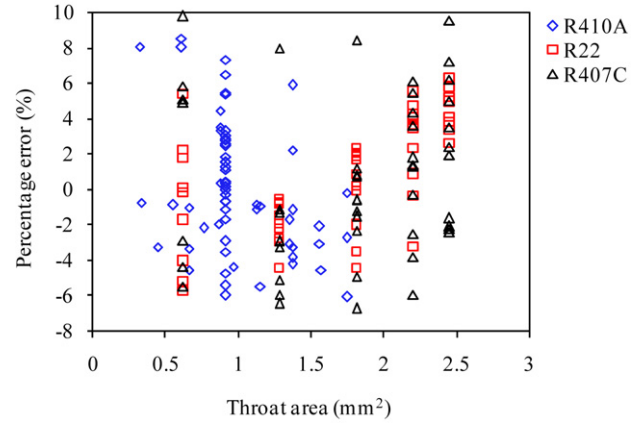**Fig. 9.** Relative deviation versus upstream pressure.

Fig. 11. Relative deviation versus throat area.

The predictions obtained by using the model were compared with the test data for each refrigerant. By the calculations of Eqs. (9), (10) and (11), the average deviations are 0.02% for R410A, 0.72% for R22, and 0.40% for R407C, respectively. The standard deviations are 3.76% for R410A, 3.22% for R22, and 4.46% for R407C, respectively. In order to analyze the applicability of the new model, the changes of the relative deviations with the measured mass flow rate, operation condition and throat area are graphically shown in Figs. 8–11. As can be seen, all the relative deviations are distributed within a range from -7% to $+10\%$, and approximately 95% of the experimental data fall within a relative deviation of $\pm 7.0\%$. The relative deviations of R410A are from -6.09% to $+8.52\%$ for the mass flow rate from 55.7 to 325.5 $\mathrm{kg\,h}^{-1}$ under the conditions of the upstream pressures from 2.10 to 3.60 MPa, the subcoolings from 2 to 22 °C, and the throat areas from 0.32 to 1.75 mm^2. For R22 and R407C, the relative deviations are from -5.75% to $+6.24\%$ and from -6.75% to $+9.75\%$, respectively, for the mass flow rate from 55.9 to 264.8 $\mathrm{kg\,h}^{-1}$ under the conditions of the upstream pressures from 1.14 to 1.96 MPa, the subcoolings from 2 to 15 °C, and the throat areas from 0.62 to 2.45 mm^2. In general, the predicting mass flow rates agree well with the experimental data.

Uncertainties exist in all of physical measurements, the aim of the uncertainty analysis for the mass flow correlation is to verify the robustness under various parameter uncertainties. The uncertainty of $\dot{m}$ is represented in terms of the parameter sensitivity, having the following form:

$$\delta\dot{m} = \sqrt{\left(\frac{\partial\dot{m}}{\partial P_{\mathrm{up}}}\right)^2 \delta P_{\mathrm{up}}^2 + \left(\frac{\partial\dot{m}}{\partial P_{\mathrm{th}}}\right)^2 \delta P_{\mathrm{th}}^2 + \left(\frac{\partial\dot{m}}{\partial \rho_l}\right)^2 \delta\rho_l^2 + \left(\frac{\partial\dot{m}}{\partial A_{\mathrm{th}}}\right)^2 \delta A_{\mathrm{th}}^2}$$

(12)

where $\delta\dot{m}$ is the uncertainty of $\dot{m}$, δP_{th} is the uncertainty of P_{th} and expressed as

$$\delta P_{\mathrm{th}} = \sqrt{\left(\frac{\partial P_{\mathrm{th}}}{\partial P_{\mathrm{up}}}\right)^2 \delta P_{\mathrm{up}}^2 + \left(\frac{\partial P_{\mathrm{th}}}{\partial T_{\mathrm{sc}}}\right)^2 \delta T_{\mathrm{sc}}^2 + \left(\frac{\partial P_{\mathrm{th}}}{\partial \rho_l}\right)^2 \delta\rho_l^2 + \left(\frac{\partial P_{\mathrm{th}}}{\partial \mu_l}\right)^2 \delta\mu_l^2 + \left(\frac{\partial P_{\mathrm{th}}}{\partial D_e}\right)^2 \delta D_e^2}$$

(13)

The uncertainty of $\dot{m}$ changes with the operating conditions, and all the experimental operating condition ranges are listed in Table 2. The uncertainties of pressure and temperature are given in Table 1, the uncertainties of ρ and μ are 0.05% and 1.5%, respectively, given by the calculation accuracy of the REFPROP [25], and the uncertainty of the orifice diameter of EEV is less than ± 0.02 mm. Consequently, by utilizing Eqs. (12) and (13), the maximum uncertainty of the calculated mass flow rate is obtained as 5.1%.

The measured data of EEV #4 in Table 2 adopted in the present model were also used to develop an conventional empirical correlation of mass flow rate by Zhang et al. [9]. The relative deviations of Zhang's modeling results to the measured data were reported as from -10.74% to 9.26% for R22 and from -14.20% to 22.10% for R407C. The main reason for the larger discrepancies is the factor that the downstream pressure P_{down}, although independent of the mass flow rate in common operating conditions, was selected in his model. This paper, taking metastability into account, conducted an experimental study on the mass flow characteristics in EEVs, and employed Bernoulli equation properly for the mass flow rate calculation without considering the two-phase flow downstream. The relative deviations of R22 and R407C are far less than the Zhang's model. It can be inferred that the complicated two-phase

flow downstream has a great influence on the predicting accuracy of the conventional model without considering metastability in EEVs. The model comparison showed that consideration of the actual flashing mechanisms in EEVs is necessary for improving the accuracy of flow models.

7. Conclusions

The mass flow characteristics of EEVs were experimentally investigated with R410A, R22 and R407C as working fluids. The metastability in EEV is an important feature under flow choking conditions. According to the experimental analyses, the metastable pressure at the throat of EEV is dependent on upstream pressure, subcooling, thermophysical properties and throat area. Based on the measured data in a wide range of operating conditions, a new model was developed using Bernoulli equation in which the metastable pressure was employed in a power law form of the dimensionless Pi-groups. The model yields the relative deviations within a range between -7% and $+10\%$, and approximately 95% of the measured data fall within a relative deviation of $\pm7.0\%$. In addition, the model has comparative advantages relative to other models without considering the actual flashing mechanisms in terms of theoretical basis and predicting accuracy.

It is notable that the present model can theoretically be used for other types of expansion valves, such as TXV and metering manual expansion valve, due to the similar structure of flow channels. However, there is an operational difficulty to determine the opening, namely the throat area, of the other expansion valves in refrigeration systems.

References

[1] C. Aprea, R. Mastrullo, Experimental evaluation of electronic and thermostatic expansion valves performances using R22 and R407C, Applied Thermal Engineering 22 (2002) 205–218.

[2] R. Lazzarin, M. Noro, Experimental comparison of electronic and thermostatic expansion valves performances in an air conditioning plant, International Journal of Refrigeration 31 (2008) 113–118.

[3] J.M. Choi, Y.C. Kim, The effects of improper refrigerant charge on the performance of a heat pump with an electronic expansion valve and capillary tube, Energy 27 (2002) 391–404.

[4] D.D. Wile, The measurement of expansion valve capacity, Refrigeration Engineering 8 (1935) 108–112.

[5] S.W. Ma, C. Zhang, J.P. Chen, Z.J. Chen, Experimental study on mass flow rate coefficient of electronic expansion valve, Journal of Shanghai Jiaotong University 39 (2) (2005) 247–250.

[6] C. Zhang, Research on characteristics of electronic expansion valve and valve head compensation to middle-small refrigeration systems, Ph.D. thesis, Shanghai Jiaotong University, China, 2006.

[7] C. Park, H. Cho, Y. Lee, Y. Kim, Mass flow characteristics and empirical modeling of R22 and R410A flowing through electronic expansion valves, International Journal of Refrigeration 30 (8) (2007) 1401–1407.

[8] A. Davies, T.C. Daniels, Single and two-phase flow of dichlorodifluoromethane through sharp-edge, ASHRAE Transaction 79 (1973) (Part I).

[9] C. Zhang, S.W. Ma, J.P. Chen, Z.J. Chen, Experimental analysis of R22 and R407c flow through electronic expansion valve, Energy Conversion and Management 47 (5) (2006) 529–544.

[10] J. Liu, J.P. Chen, Q.F. Ye, Z.J. Chen, A new model for depicting mass flow rate characteristic of electronic expansion valves, Experimental Thermal and Fluid Science 32 (2007) 214–219.

[11] Y. Kim, D.L. O'Neal, An experimental study of two-phase flow of HFC-134a through short tube orifices, Heat Pump and Refrigeration Systems Design, Analysis, and Applications, AES–ASME 29 (1993) 1–8.

[12] V.E. Schrock, E.S. Starkman, R.A. Brown, Flashing flow of initially subcooled water in convergent-divergent nozzles, ASME Journal of Heat Transfer 99 (1977) 263–268.

[13] M.D. Alamgir, J.H. Lienhard, Correlation of pressure undershoot during hot water depressurization, ASME Journal of Heat Transfer 103 (1981) 52–55.

[14] N. Abuaf, O.C. Jones, B.J.C. Wu, Critical flashing flows with subcooled inlet conditions, J. Heat Transfer, Trans. ASME 105 (1983) 379–383.

[15] M.M. Vieira, J.R. Simões-Moreira, Low-pressure flashing mechanisms in iso-octane liquid jet, Journal of Fluid Mechanics 572 (2007) 121–144.

[16] J.R. Simões-Moreira, C.W. Bullard, Pressure drop and flashing mechanisms in refrigerant expansion devices, International Journal of Refrigeration 26 (2003) 840–848.

[17] J.R. Simões-Moreira, Oblique evaporation waves, Shock Waves 10 (2000) 229–234.

[18] D.A. Aaron, P.A. Domanski, Experimentation, analysis, and correlation of R-22 flow through short tube restrictors, ASHRAE Trans. 96 (1) (1990) 729–742.

[19] R.A. Brown, Flashing expansion of water through a converging-diverging nozzle, M.S. thesis, University of California, Berkeley, USAEC Report UCRL-6665-T, 1961.

[20] G.L. Sozzi, W.A. Sutherland, Critical flow of saturated and subcooled water at high pressure, General Electric Company Report NEDO-13418, 1975.

[21] G.A. Zimmer, B.J.C. Wu, W.L. Leonhard, N. Abuaf, O.C. Jones, Pressure and void distributions in a converging-diverging nozzle with non-equilibrium water vapor generation, BNL-NUREG-26003, 1979.

[22] J.R. Simoneau, R.C. Hendricks, Two-phase choked flow of cryogenic fluids in converging-diverging nozzles, NASA Technical Paper 1484, July 1979.

[23] ASHRAE Standard 41.1, Standard method for temperature measurement, ASHRAE, Atlanta (GA), 1986.

[24] ASHRAE Standard 41.3, Standard method for pressure measurement, ASHRAE, Atlanta (GA), 1989.

[25] M.O. McLinden, S.A. Klein, E.W. Lemmon, A.P. Peskin, NIST thermodynamic and transport properties of refrigerants and refrigerant mixtures (REFPROP), Version 6.0, National Institute of Standards and Technology, Gaithersburg, MD, 1998.

[26] E. Buckingham, On physically similar systems: illustrations of the use of dimensional equations, Phys. Rev. 4 (4) (1914) 345–376.